Nonlinear vibration isolator with adjustable restoring force

Yoshikazu Araki[a*], Takehiko Asai[b], Kosuke Kimura[a], Kosei Maezawa[c], Takeshi Masui[d]

[a]*Department of Architecture and Architectural Engineering, Kyoto University, Katsura, Nishikyo, Kyoto 615-8540, Japana*

[b]*Department of Civil and Environmental Engineering, University of Illinois at Urbana-Champaign, 205 N. Mathews Ave., Urbana, IL 61801, USA*

[c]*Hojo Structure Research Institute, Kawaracho, Chuo, Osaka 541-0048, Japan*

[d]*Department of Architecture, Kansai University, Yamatecho, Suita, Osaka 564-8680, Japan*

Email Address: araki@archi.kyoto-u.ac.jp (Yoshikazu Araki)

Abstract

This paper presents a vertical quasi-zero stiffness (QZS) vibration isolator with a mechanism for adjusting restoring force. QZS vibration isolators have high initial stiffness and QZS around the static equilibrium position. This way, excessive deformation due to self-weight can be avoided while having enough vibration reduction capability to dynamic excitations. One of the main issues left for QZS vibration isolators is the difficulty in keeping the vibration reduction capability when the vibration isolated object is replaced. In such a case, adjustment of its restoring force becomes necessary in accordance with the self-weight of the newly placed vibration isolated object. This paper attempts to address this issue by proposing a mechanism that enables quick and easy adjustment of the restoring force of a QZS vibration isolator. The proposed mechanism consists of cranks and a screw jack. With the present

1

25 mechanism, the restoring force provided by horizontally placed springs can be

26 converted into the vertical restoring force of the vibration isolator. In the conversion, the

27 vertical resisting force can be adjusted simply by applying and removing torque to the

28 screw jack to change and hold the angle of inclined bars placed in the cranks. In this

29 study, a prototype of a class of QZS vibration isolator having the proposed mechanism

30 is produced. Shaking table tests are performed to demonstrate the efficacy of the present

31 mechanism, where the produced prototype is subjected to various sinusoidal and

32 earthquake ground motions. It is demonstrated through the shaking table tests that the

33 produced prototype can reduce the response acceleration within the same tolerance even

34 when the mass of the vibration isolated object is changed.

35

38

1. Introduction

40 Passive vibration isolation has been an active area of research, and a variety of passive

41 vibration isolators have been developed so far. For horizontal vibration isolation, low

42 stiffness elements such as springs are installed between the base of a vibration isolator

43　and the objects to be isolated. The low stiffness elements prevent vibration energy from

44　being transmitted into the isolated object. On the other hand, if low stiffness elements

45　are used for vertical vibration isolation, large deformations take place due to the

46　self-weight of the isolated objects. This makes vertical vibration isolation much more

47　difficult than horizontal vibration isolation.

48　　　　To overcome the difficulty, quasi-zero-stiffness (QZS) vibration isolators have

49　been studied for many years [1-25]. QZS vibration isolators are designed so that their

50　restoring forces satisfy the following two conditions: (1) initial stiffness, which resists

51　self-weight, is large, and (2) the tangent stiffness, which resists dynamic load, is close to

52　zero around the static equilibrium position. This way, transmission of vibration energy

53　due to dynamic load can be prevented while excessive deformation due to self-weight

54　can be avoided. In most QZS vibration isolators, such nonlinear restoring forces are

55　realized by effective use of geometric nonlinearity [1-22]. In the past studies, magnets

56　[23,24] or shape memory alloys [25] were also used to obtain such nonlinear restoring

57　forces.

58　　　　One of the main issues left for the QZS vibration isolators is the difficulty in

59　adjusting their restoring forces to the change of the self-weight, or the mass, of the

60　isolated object. When the mass changes, it is necessary for the QZS vibration isolators

61   to adjust their restoring force by, e.g., replacing springs. The use of balance weight is

62   another way of dealing with the mass change. In either case, it is not easy and takes

63   considerable time for the adjustment of the nonlinear restoring force of a QZS vibration

64   isolator. To the authors' knowledge, however, no studies have addressed this issue.

65   This study presents a QZS vibration isolator with a mechanism that enables easy

66   and quick adjustment of its nonlinear restoring force. In this paper, first, a mechanism is

67   proposed to change the nonlinear restoring force. Also presented is a combination of the

68   proposed mechanism and a vertical vibration isolator with flag-shaped restoring force,

69   which belongs to a class of QZS vibration isolators and was proposed in the authors'

70   previous work [26,27]. To show the efficacy of the present mechanism, a prototype of

71   the proposed vibration isolator is produced to perform quasi-static and dynamic loading

72   tests. Numerical simulations are also conducted to compare the test and simulation

73   results with theoretical predictions.

74

75   **2. Mechanisms**

76   *2.1. Mechanism for adjusting restoring force*

77   Figure 1(a) illustrates a schematic view of the present vibration isolator. As shown in

78   Figure 1(b), the proposed isolator is divided into three portions. The upper portion is a

79   table on which the isolated objects are placed. The upper portion consists of one

80   horizontal top plate and two vertical hexagonal plates. The middle portion is composed

81   of two shafts connected by elements to provide a nonlinear restoring force.

82   Constant-force springs, coil springs, and wires are examples of such elements. Here,

83   constant-force springs are composed of rolled spring steel and have constant restoring

84   force regardless of their stretch [26,27]. At both ends of each shaft, inner and outer

85   roller bearings are installed. In the lower portion, one screw jack, two linear bushes, and

86   four cranks are attached to the base plate. Here, the screw jack and the linear bushes are

87   connected by two beams. The beams are connected to the cranks using pin connections.

88   Half of the length of the screw jack is threaded in the opposite direction to that of the

89   other half. The distance between the two beams can be changed by rotating the screw

90   jack while keeping the geometry of the mechanism symmetric. The positions of the

91   beams are automatically locked simply by removing the torque applied to the screw jack.

92   This way, the angle of the inclined bar in each crank can be changed and held simply by

93   applying and removing the torque to the screw jack. As depicted in Figure 1(a), the

94   inclined sides of the hexagonal plates are placed on the inner bearings of the shafts, and

95   the outer bearings of the shafts are placed on the inclined bars of the cranks. With such a

96   composition, the horizontal restoring force provided by the middle portion can be

97   converted into the vertical restoring force. In the conversion, furthermore, the vertical

98   resisting force can be adjusted simply by changing the angle of the inclined bars of the

99   cranks, which is the key ingredient of the present vibration isolator.

100   The relationship between the restoring force f of the vibration isolator and the

101   restoring force n provided by the middle portion shown in Figure 2 is derived below.

102   Here, the positive direction of f is compression while that of n is tension. As shown in

103   Figures 2(b) and 2(c), let the angles of bar AB and the inclined side of the upper table

104   be θ and γ, respectively, with respect to the vertical. Figure 3 illustrates the internal

105   forces acting on the right shaft shown in Figure 2(b). Figure 3(a) illustrates the internal

106   force acting on each inner bearing from the inclined side of the upper table. Figure 3(b)

107   shows the internal force acting on each outer bearing from inclined bar AB of the crank.

108   As shown in Figure 3(c), the force-balance equation in the horizontal direction for the

109   shaft can be written as

110
$$n = \frac{1}{2}\left(\frac{1}{\tan\theta} + \frac{1}{\tan\gamma} \right) f \,. \tag{1}$$

111   Assume that the mass of the shaft is negligibly small. Then, Eq. (1) is valid even under

112   dynamic condition. Thus, the amplification factor α is defined as

113
$$\alpha(\theta) = \frac{f}{n} = \frac{2}{1/\tan\theta + 1/\tan\gamma} \,. \tag{2}$$

114   Figure 2(c) illustrates the schematic view of a crank. Bars AB and AE are connected by

115   a pin at point A. Bars CD and AB are also connected by a pin at point D. Bar AE is

116   connected rigidly to the base plate at point E. The lengths of AD, AE, and CD are r, s,

117   and l, respectively. Let h indicate the distance between point C and the base plate. Let

118   the distance between point C and bar AE be d, which is the key variable to adjust θ.

119   Then, the geometric relationship between θ and d is

120   $$l^2 = (d + r\sin\theta)^2 + (s - h - r\cos\theta)^2. \tag{3}$$

121   Suppose that d is given. Then, θ can be calculated by solving Eq. (3), and α can be

122   obtained by substituting the calculated θ into Eq. (2).

123

124   *2.2. Mechanism for flag-shaped restoring force*

125   Figure 4 shows a mechanism for providing a flag-shaped restoring force [26,27]. The

126   relative vertical displacement between the upper table and the base is defined as u,

127   whose positive direction is contraction. The relative displacement between the two

128   shafts is defined as w, whose positive direction is extension. Figure 4(a) depicts the

129   position where the upper table is at the upper limit of the stroke of the vibration isolator.

130   At this position, both u and w are set as $u=w=0$. Figures 4(b) illustrates the static

131   equilibrium position when an object is placed on the upper table, where $u=u_{se}$ and

132   $w=w_{se}$. Here, m denotes the mass of the object and g indicates the gravitational

7

133   acceleration. Figure 4(c) illustrates the position where the upper table reaches the lower

134   limit of the stroke, where $u=u_{max}$ and $w=w_{max}$.

135   In the following, the variation of n is considered when w is increased from 0 to

136   w_{max}. When $w=0$, the restoring force n changes from 0 to N_1, where N_1 is the sum of the

137   capacities of constant-force springs 1a and 1b. At all the positions when $0<w<w_{max}$, both

138   constant-force springs 1a and 1b provide restoring forces equal to their capacities. On

139   the other hand, constant-force spring 2, which is connected to the shafts via a coil spring

140   and a wire in series, provides a restoring force between 0 and N_2, where N_2 denotes the

141   capacity of constant-force spring 2. When w is small, no restoring force is provided by

142   constant-force spring 2 due to the sag of the wire. In this case, n is expressed as $n=N_1$.

143   When the upper tables moves downward beyond the position where the wire sag stops

144   to take place, the length of the coil spring changes linearly with respect to w. The

145   present vibration isolator is designed so that the static equilibrium position lies in this

146   linear range. Here, the coil spring is used to avoid high frequency accelerations caused

147   by sudden, or discontinuous, change of the restoring force. When the upper table moves

148   downward further and exceeds the position where the restoring force of the coil spring

149   reaches N_2, the restoring force provided by constant-force spring 2 becomes N_2. In this

150   case, n is expressed as $n= N_1+ N_2$.

151   Figures 5(a) and 5(b) illustrate the *f-u* and *n-w* relationships. These figures also

152   illustrate the shifts of axes. In this paper, $\Delta(\,\bullet\,)$ indicates that the reference position

153   of the variable is the static equilibrium position. More specifically, Δf, Δn, Δu, and

154   Δw are defined as

155 $$\Delta f = f - mg, \quad \Delta n = n - mg/\alpha, \quad \Delta u = u - u_{se}, \quad \Delta w = w - w_{se}. \tag{4}$$

156   Such shifts of axes are introduced here to consider the vibration around the static

157   equilibrium position. Figure 5(c) depicts the geometric relationship between *u* and *w*

158   when the upper table is moved downward while the base is fixed. The thicker line

159   indicates the upper side of bar AB, and the thinner lines indicate the inclined side of the

160   upper table before and after the movement. From this figure, the geometric relationship

161   can be written as

162 $$u = \frac{1}{2}\left(\frac{1}{\tan\gamma} + \frac{1}{\tan\theta}\right)w = \frac{1}{\alpha}w. \tag{5}$$

163   Figure 6(a) shows the relationship between the shifted restoring force Δn_{NF} and

164   the shifted relative displacement Δw, where no friction is assumed. Let *k* be the

165   stiffness of the coil spring. Then, the relationship can be written as

166 $$\Delta n_{NF} = n_{NF} - \frac{mg}{\alpha} = \begin{cases} N_1 - mg/\alpha & \text{if} & -w_{se} < \Delta w < w_L \\ k\Delta w & \text{if} & \Delta w_L \le \Delta w \le \Delta w_U \\ N_1 + N_2 - mg/\alpha & \text{if} & w_U < \Delta w < w_{\max} - w_{se} \end{cases}, \tag{6}$$

167   where

9

168
$$\Delta w_U = \left(N_1 + N_2 - mg/\alpha \right)/k, \quad \Delta w_L = \left(N_1 - mg/\alpha \right)/k. \qquad (7)$$

169   Figure 6(b) illustrates the relationship between the friction force q and $\Delta \dot{w}$ assuming

170   Coulomb's friction [28]. Here, the overdot indicates the differentiation with respect to

171   time. The friction force q can be written as

172
$$q = \begin{cases} -Q & \text{if} \quad \Delta \dot{w} < 0 \\ 0 & \text{if} \quad \Delta \dot{w} = 0 \\ Q & \text{if} \quad \Delta \dot{w} > 0 \end{cases}. \qquad (8)$$

173   Then the shifted restoring force Δn including Coulomb's friction can be written as

174
$$\Delta n(\Delta w, \Delta \dot{w}) = \Delta n_{NF}(\Delta w) + q(\Delta \dot{w}), \qquad (9)$$

175   Figure 7 illustrates this relationship. The restoring force curve shown in Figure 7(c) is

176   called as "flag-shaped restoring force" because the shape of the restoring force curve in

177   the region of $\Delta n > 0$ and $\Delta w > 0$ looks like a flag [29].

178   From Eq. (2), the relationship between Δn and Δf can be written as

179
$$\Delta f = \alpha \Delta n. \qquad (10)$$

180   And, from Eq. (5), the relationship between Δu and Δw can be written as

181
$$\Delta u = \frac{1}{\alpha} \Delta w. \qquad (11)$$

182   From Eqs. (10) and (11), Δf can be written as

183
$$\Delta f(\Delta u, \Delta \dot{u}) = \begin{cases} \alpha \left(N_1 + q(\alpha \Delta \dot{u}) \right) - mg & \text{if} \quad -u_{se} < \Delta u < w_L/\alpha \\ \alpha^2 k \Delta u + \alpha q(\alpha \Delta \dot{u}) & \text{if} \quad w_L/\alpha \le \Delta u \le w_U/\alpha \\ \alpha \left(N_1 + N_2 + q(\alpha \Delta \dot{u}) \right) - mg & \text{if} \quad w_U/\alpha < \Delta u < u_{max} - u_{se} \end{cases}, \qquad (12)$$

10

184   Note that, when *mg* changes, α should be adjusted so that the following inequality

185    $$\alpha\left(N_1+Q\right)<mg<\alpha\left(N_1+N_2-Q\right), \text{ or } \frac{mg}{N_1+N_2-Q}<\alpha<\frac{mg}{N_1+Q} \qquad (13)$$

186   holds to make the vibration isolator self-centering, or to make the upper table return to

187   the static equilibrium position when the external force other than the gravity force is

188   removed.

189   The strengths of the present mechanism and the flag-shaped restoring force can be

190   summarized as follows:

191   1. The use of constant-force springs allows the mechanism to have a long stroke of

192   more than several centimeters while keeping the mechanism compact.

193   2. Existence of plateau in the restoring force curve limits the response acceleration

194   within a specified tolerance regardless of the amplitude and frequency of an input

195   motion.

196   3. The flag-shaped restoring force provides the isolator with the self-centering

197   capability. This is because static equilibrium can be achieved only at the origin of

198   the restoring force curve. The self-centering capability prevents the displacement

199   from accumulating in one direction in vibration, which may be seen when friction

200   damping is applied [29].

201   4. The flag-shaped restoring force avoids resonance. The proposed isolator responses

11

202   linearly in the neighborhood of the static equilibrium point. In this linear range, the

203   isolator has a potential of resonance. Nevertheless, this does not lead to serious

204   problems because the displacement amplitude of interest in this paper is well

205   beyond the linear range. Even if resonance takes place in the linear range, the

206   equivalent natural frequency (computed either by the secant stiffness or by the

207   tangent stiffness) decreases significantly as the displacement amplitude increases

208   beyond the linear range. The change of the equivalent natural frequency with

209   respect to the displacement amplitude avoids resonance.

210

211   *2.3. Upper bound of response acceleration*

212   As pointed out in Section 2.2, one of the key features of the present vibration isolator is

213   that it can limit the response acceleration within a specified tolerance regardless of the

214   magnitude and frequency of an input motion. This subsection presents basic equations

215   for this feature. Suppose that the vibration isolator is subject to the (absolute) ground

216   acceleration $\ddot{u}_g$. Then, the equation of motion for the present vibration isolator can be

217   written as

218   $$m\left(\Delta\ddot{u} + \ddot{u}_g\right) + c\Delta\dot{u} + \Delta f\left(\Delta u, \Delta\dot{u}\right) = 0. \tag{14}$$

219   Assume that the vibration isolator is designed so that c is negligibly small. Then, from

220   Eqs.(8), (12), and (14), the magnitude of the absolute response acceleration $\left| \Delta \ddot{u} + \ddot{u}_g \right|$

221   can be bounded as

222 $$\left| \Delta \ddot{u} + \ddot{u}_g \right| \leq h(\alpha), \tag{15}$$

223   where

224 $$h(\alpha) = \max\left(g - \frac{\alpha}{m}(N_1 - Q), \frac{\alpha}{m}(N_1 + N_2 + Q) - g \right). \tag{16}$$

225   From Eqs. (15) and (16), it can be said that the proposed vibration isolator can specify

226   the peak response accelerations by adjusting α / m. This implies that the present

227   vibration isolator can reduce the peak response acceleration to the same value by

228   adjusting the amplification factor α when m is changed.

229   Consider the range of variation of $h(\alpha)$ when α changes in the range of Eq. (13).

230   Both $g - \alpha(N_1 - Q)/m$ and $\alpha(N_1 + N_2 + Q)/m - g$ are linear functions of α, and

231   hence $h(\alpha)$ is a piecewise linear function of α. The range of variation of $h(\alpha)$ can be

232   obtained as

233 $$\frac{N_2/2 + Q}{N_1 + N_2/2} g \leq h(\alpha) < \frac{N_2}{N_1 + Q} g. \tag{17}$$

234   It should be noted here that, from Eqs. (15) to (17), the response acceleration can be

235   reduced to less than $N_2 g / (N_1 + Q)$ regardless of m as far as the assumptions made in

236   this section are valid.

237

238   ## 3. Experiments

239   ### 3.1 Prototype design

240   Figure 8 shows a photograph of a prototype of the present vibration isolator produced

241   for testing the effectiveness of the proposed mechanisms. The height of the vibration

242   isolator at the static equilibrium position is about 400 mm. To suppress the rocking

243   response of the upper table, 2 plates are fixed with pin connections to each side of the

244   vibration isolator. Note that, although the screw jack is rotated by hand in the present

245   prototype of the vibration isolator, it is possible to use a combination of sensing devices

246   and an electric motor to rotate the screw jack for sensing the mass change and adjusting

247   the restoring force automatically.

248   The parameters for the mechanism for the flag-shaped restoring force are as

249   follows. The nominal values of N_1 and N_2 are 235.5 N and 31.4 N, respectively, and that

250   of k is 1.5 N/mm. It is difficult to determine the value of Q prior to the quasi-static

251   loading tests because friction takes place at many locations. Hence, as explained later in

252   Section 3.2, the reference value of Q is determined as 6.8 N from the quasi-static

253   loading tests. Substituting these values into Eq. (17), the theoretical prediction of the

254   upper bound of the response acceleration can be obtained as 0.13 g.

255   The parameters for the mechanism for changing the restoring force are provided

256   as $\tan\gamma = 1.6$, l = 150 mm, r = 75 mm, and $s - h$ = 150 mm. Figure 9 shows the

257   relationship between the amplification factor α and d. Here, recall that d is the

258   distance between point C and bar AE as shown in Figure 2. Table 1 shows the reference

259   values that define the amplified restoring forces, where $N_{1(\alpha)}$, $N_{2(\alpha)}$, $Q_{(\alpha)}$, $u_{R(\alpha)}$, and

260     $k_{(\alpha)}$ are defined as

261 $$N_{1(\alpha)} = \alpha N_1, \quad N_{2(\alpha)} = \alpha N_2, \quad Q_{(\alpha)} = \alpha Q, \quad u_{R(\alpha)} = \frac{w_U - w_L}{\alpha}, \quad k_{(\alpha)} = \alpha^2 k. \qquad (18)$$

262

263   *3.2 Quasi-static loading tests*

264   To obtain the parameters for constructing a numerical model of the proposed vibration

265   isolator, quasi-static loading tests are carried out. The quasi-static loading tests are

266   performed by changing the value of d parametrically from 15 mm to 65 mm with an

267   increment of 5 mm. In each quasi-static loading test, forced displacement is applied to

268   the upper table manually. The origin is set to the equilibrium position for each test. The

269   displacement of the upper table is obtained by using non-contact laser displacement

270   sensors. The restoring force *f* is obtained by the load cells inserted between the ground

271   and the base of the vibration isolator.

272   Figure 10(a) shows the restoring force curves obtained from the quasi-static

273   loading tests for the cases of d = 60, 40, and 20 mm. Here, the results are shown only

274   for the region of $-50\text{mm} < \Delta u < 50\text{mm}$ while the applied displacement amplitude of

275   Δu was more than 50mm. From the figure, it is clear that the restoring force is

276   amplified by adjusting the value of d. Figure 10(b) shows the numerical models of the

277   restoring force curves, where $S_{1(\alpha)}$ and $S_{2(\alpha)}$ are the upper and lower values of the

278   restoring force when $\Delta u \le -u_{R(\alpha)}/2$, and $S_{3(\alpha)}$ and $S_{4(\alpha)}$ are the values when

279     $u_{R(\alpha)}/2 \le \Delta u$. Table 2 summarizes the values of the parameters that determine the

280   flag-shaped restoring force. The procedure used for determining these values is

281   summarized as follows:

282   1.   The values of $S_{1(\alpha)}$ and $S_{2(\alpha)}$ are determined by averaging the upper and lower

283   values of the restoring force curve, respectively, in the range of

284        $-50 \text{ mm} \le \Delta u \le -u_{R(\alpha)}/2$. The values of $S_{3(\alpha)}$ and $S_{4(\alpha)}$ are determined similarly

285   in the range of $u_{R(\alpha)}/2 \le \Delta u \le 50 \text{ mm}$.

286   2.   The amplified capacities $N_{1(\alpha)}$ and $N_{2(\alpha)}$ are obtained as

287
$$N_{1(\alpha)} = \frac{S_{1(\alpha)} + S_{2(\alpha)}}{2}, \quad N_{2(\alpha)} = \frac{S_{3(\alpha)} + S_{4(\alpha)}}{2} - N_{1(\alpha)}. \tag{19}$$

288   3.   The amplified stiffness $k_{(\alpha)}$ around the static equilibrium position is determined

289   by

290
$$k_{(\alpha)} = \frac{N_{2(\alpha)}}{u_{R(\alpha)}}. \tag{20}$$

291   4.   The amplified friction force $Q_{(\alpha)}$ is determined by

292
$$Q_{(\alpha)} = \frac{\left(S_{1(\alpha)} - S_{2(\alpha)}\right) + \left(S_{3(\alpha)} - S_{4(\alpha)}\right)}{2} . \tag{21}$$

293   The experimentally observed restoring force curves shown in Figure 10(a) are not so

294   smooth as their numerical models shown in Figure 10(b) because it is difficult to realize

295   such ideal restoring force curves shown in Figure 9(b) due to many factors. Uncertainty

296   of the restoring force provided by the constant-force springs is one of the main reasons.

297   Backlash and friction in the bearings and pin-connections are other obstacles to realize

298   such ideal restoring force curves.

299   Figure 11 compares the nominal values of $N_{1(\alpha)}$ and $N_{2(\alpha)}$ with those obtained

300   experimentally. Good agreement can be seen between these values. In Figure 12, the

301   cross mark plots the relationship between $N_{1(\alpha)}$ and $Q_{(\alpha)}$, both of which are obtained

302   from the experiments. The solid line shows the linear relationship

303
$$Q_{(\alpha)} = \beta N_{1(\alpha)}, \tag{22}$$

304   where the value of β is obtained by the least-squares fit as 0.029. The reference value

305   $Q_{(\alpha)}$ shown in Table 1 is obtained by multiplying the obtained value of β and the

306   nominal value of $N_{1(\alpha)}$.

307

308   *3.3. Shaking table tests*

17

309   Figure 13 illustrates the configuration of the experimental setup. Only vertical ground

310   motions are applied to the vibration isolator. To investigate the vibration reduction

311   capability of the present vibration isolator when the mass of the isolated object is

312   changed, shaking table tests are performed for the cases of d = 60, 40, and 20 mm.

313   These values correspond to the amplification factor α of 1.25, 1.57, and 1.91, and the

314   mass m of 32.0 kg, 40.2 kg, and 49.0 kg, respectively. Acceleration sensors are installed

315   on the upper table of the vibration isolator to measure response acceleration (RA), and

316   on the shaking table to record ground acceleration (GA). Non-contact laser

317   displacement sensors are fixed to a measurement frame to measure response absolute

318   displacement (RAD) and ground displacement (GD). Response relative displacement

319   (RRD) is obtained by subtracting GD from RAD. The primary natural frequencies in the

320   neighborhood of the static equilibrium position are 2.74, 3.26, and 3.68 Hz for the cases

321   of d = 60, 40, and 20 mm, respectively. These values are obtained from the free

322   vibration measurements.

323   Table 3 summarizes input excitations. The input waves are 2, 3, 4, 5, and 6 Hz

324   sine waves, and the vertical, or up-down (UD), component of the earthquake ground

325   motion recorded at K-NET Ojiya station in Japan during the 2004 Mid Niigata

326   Prefecture earthquake. The peak ground accelerations (PGAs) are normalized to 0.25 g

327   and 0.50 g for 2 Hz sine wave, 0.25 g, 0.50 g, 0.75 g, and 1.00 g for 3, 4, 5, and 6 Hz

328   sine waves. The PGAs are normalized to 0.50 g, 0.75 g, and 1.00 g for the K-NET Ojiya

329   UD earthquake ground motion, whose PGA is 0.83 g.

330   Table 4 reports all the PGAs and the peak response accelerations (PRAs)

331   measured in the shaking table tests. Due to the limitations of the capability of the

332   shaking table, there are small differences between the intended and the measured PGAs.

333   Figure 14 compares the PRAs with the PGAs. As can be observed in Table 4 and Figure

334   14, the PRAs are reduced to under 0.2 g for all the sine waves except the case of $d = 20$

335   mm and S4-4 input. On the other hand, the PRAs were dropped to under 0.15 g for all

336   the scaled earthquake ground motions. These results demonstrate that the proposed

337   vibration isolator can reduce the response acceleration effectively in a wide range of

338   input frequency and amplitude. Table 5 summarizes the peak response absolute

339   displacements (PRADs) and the peak ground displacements (PGDs). It is seen in Table

340   5 that significant reduction was achieved in PRAD to all sine waves. On the other hand,

341   reductions are not observed for the K-Net Ojiya UD records. In fact, the PRADs were

342   amplified by the vibration isolator. Figure 15 shows examples of the time histories of

343   the GA, RA, GD, RAD, RRD for the case of $d = 40$ mm. The input excitations are S4-4

344   and O-3. Figure 15 shows that the RAs were reduced sufficiently during the entire

19

345   excitation for both cases. The reduction of the RAD to S4-4 excitation and the

346   amplification to O-3 excitation were confirmed through the plots of the time histories.

347

348   **4. Numerical Simulations**

349   In this section, numerical simulations are performed to compare their results with the

350   experimental results. For the numerical simulations, the values of $N_{1(\alpha)}$, $N_{2(\alpha)}$, $Q_{(\alpha)}$,

351   and $k_{(\alpha)}$ obtained from the quasi-static loading tests (shown in Table 2) are used. The

352   values of the mass used in the shaking table test are substituted into m, i.e., 32.04 kg,

353   40.24 kg, and 48.95 kg for the cases of $d = 60$ mm, 40 mm, and 20 mm, respectively.

354   The damping factor c is assumed to be 0.01 Ns/mm for $d = 60$ mm, 0.04 Ns/mm for $d =$

355   40 mm, and 0.06 Ns/mm for $d = 20$ mm. These values are determined by trial and error

356   to fit the simulations results to the experimental data. To avoid singular points in

357   numerical simulations, the friction force q is approximated by $q*$, defined as

358
$$q^* = \begin{cases} -Q & \text{if} & \Delta\dot{w} < -Q/b \\ b\Delta\dot{w} & \text{if} & -Q/b \le \Delta\dot{w} \le Q/b, \\ Q & \text{if} & \Delta\dot{w} > Q/b \end{cases} \tag{23}$$

359   The slope b is determined as 1 Ns/mm for all the cases by trial and error as well.

360   Numerical integrations are performed using the Runge-Kutta method.

361   Figure 16 compares the time history responses of the RAs calculated from the

20

362   simulations with the experimental results when the input excitations are S4-4 and O-3

363   and the value of d is 40 mm. Figure 16 demonstrates that the RA waves obtained from

364   the simulations agree reasonably well with the experimental results.

365   The PRAs obtained from the experiments and the simulations for the cases of $d =$

366   60, 40, and 20 mm are compared in Figure 17, where the input excitations are S2-2,

367   S3-4, S4-4, S5-4, S6-4, and O-3. For reference, the theoretical prediction of the upper

368   bound of the response acceleration obtained by using Eq. (17) is plotted by the solid line.

369   As shown in Figure 17, the theoretical prediction agrees well with the simulation results.

370   On the other hand, there are a couple of cases where the PRAs obtained from the

371   shaking table tests exceed the theoretical predictions.

372   Figure 18 compares the response acceleration spectra [30] to study the potential

373   of the measured waves to shake the objects placed on the shaking table and the upper

374   table of the isolator. In the figure, the case of S4-4 and $d = 20$ mm where the highest

375   PRA are measured is investigated and the damping ratio is assumed as 5 %. As can be

376   seen from Figure 18, the difference between the experimental and simulation results of

377   the response acceleration appears mainly in the frequency range higher than 20 Hz. This

378   verifies that the low frequency vibrations, which are important for avoiding large

379   displacement of the isolated object, are suppressed effectively by the present vibration

380   isolator, although scrutiny of the source of the unintended high-frequency vibrations is

381   still necessary. Backlash and friction in the bearings and pin-connections are potential

382   sources of the unintended high-frequency vibrations.

383

384   **5. Conclusions**

385   This study has presented a passive vertical vibration isolator with nonlinear restoring

386   force adjustable to the change of the mass of the isolated object. A simple mechanism to

387   change the nonlinear restoring force has been introduced. One of the main features of

388   the present vibration isolator is that quick and easy adjustment is possible when the

389   mass of the isolated object is changed while keeping the peak response acceleration

390   within the same tolerance. The efficacy of the proposed vibration isolator has been

391   demonstrated through shaking table tests and numerical simulations, where the vibration

392   isolator was subjected to sine waves and scaled earthquake ground motions under

393   different values of the mass of the isolated object.

394

Kyoto University, helped with the shaking table and quasi-static loading tests. The comments from the reviewers led to significant improvements of the manuscript. All the supports mentioned above are gratefully acknowledged.

References

[1]   P. Alabuzhev, A. Gritchin, L. Kim, G. Migirenko, V. Chon, P. Stepanov. *Vibration Protecting and Measuring Systems with Quasi-zero Stiffness*. Hemisphere Publishing: NY, 1989.

[2]   W.G. Molyneux. The Support of an Aircraft for Ground Resonance Tests: A Survey of Available Methods, *Aircraft Engineering and Aerospace Technology*, 30(6) (1958) 160-166.

[3]   S.E. Woodard, J.M. Housner. Nonlinear behavior of a passive zero-spring-rate suspension system, *Journal of Guidance, Control, and Dynamics*, 14(1), (1991), 84-89.

[4]   D.L. Platus. Negative-stiffness-mechanism vibration isolation systems, *Proceedings of SPIE* Vol. 1619, Vibration Control in Microelectronics, Optics, and Metrology, (1992) 44-54.

[5]   J. Winterood, D. Blair, B. Slagmolen. High performance vibration isolation using

springs in Euler column buckling mode, *Physics Letters A*, 300 (2002) 122-130.

[6] L.N. Virgin, R.B. Davis. Vibration isolation using buckled struts, *Journal of Sound and Vibration*, 260 (2003) 965–973.

[7] R.H. Plaut, J.E. Sidbury, L.N. Virgin. Analysis of buckled and pre-bent fixed-end columns used as vibration isolators, *Journal of Sound and Vibration*, 283 (2005) 1216–1228.

[8] A. Carrella, M. Brennan, T. Waters. Static analysis of a passive vibration isolator with quasi-zero-stiffness characteristic*, Journal of Sound and Vibration*, 301 (2007) 678-689.

[9] C.-M. Lee, V. Goverdovskiy, A. Temnikov. Design of springs with negative stiffness to improve vehicle driver vibration isolation, *Journal of Sound and Vibration*, 302 (2007) 865-874.

[10] R. Plaut, H. Favor, A. Jeffers, L. Virgin. Vibration isolation using buckled or pre-bent columns Part 1: Two-dimensional motions of horizontal rigid bar, *Journal of Sound and Vibration*, 310 (2008) 409-420.

[11] A.E. Jeffers, R.H. Plaut, L.N. Virgin, Vibration isolation using buckled or pre-bent columns—Part 2: Three-dimensional motions of horizontal rigid plate, *Journal of Sound and Vibration*, 310 (2008) 421–432.

434   [12] R. Ibrahim. Recent advances in nonlinear passive vibration isolators, *Journal of*

435   *Sound and Vibration*, 314 (2008) 371-452.

436   [13] I. Kovacic, M. J. Brennan, T. P.Waters. A study of a nonlinear vibration isolator

437   with a quasi-zero stiffness characteristic, *Journal of Sound and Vibration*, 315

438   (2008) 700-711.

439   [14] L.N. Virgin, S.T. Santillan, R.H. Plaut. Vibration isolation using extreme

440   geometric nonlinearity, *Journal of Sound and Vibration*, 315 (2008) 721–731.

441   [15] H.J. Ahn. Performance limit of a passive vertical isolator using a negative

442   stiffness mechanism, *Journal of Mechanical Science and Technology*, 22 (2008)

443   2357-2364

444   [16] A. Carrella, M. Brennan, I. Kovacic, T. Waters. On the force transmissibility of a

445   vibration isolator with quasi-zero-stiffness, *Journal of Sound and Vibration*, 322

446   (2009) 707-717.

447   [17] I. Kovacic, M.J. Brennan, B. Lineton. Effect of a static force on the dynamic

448   behavior of a harmonically excited quasi-zero stiffness system, *Journal of Sound*

449   *and Vibration*, 325 (2009) 870-883.

450   [18] G. Gatti, I. Kovacic, M. J. Brennan. On the response of a harmonically excited

451   two degree-of-freedom system consisting of a linear and a nonlinear quasi-zero

452   stiffness oscillator, *Journal of Sound and Vibration*, 329 (2010) 1823-1835.

453   [19] T.D. Le, K.K. Ahn. A vibration isolation system in low frequency excitation

454   region using negative stiffness structure for vehicle seat, J*ournal of Sound and*

455   *Vibration*, 330 (2011) 6311-6335.

456   [20] A. Carrella, M.J. Brennan, T.P. Waters, V. Lopes. Force and displacement

457   transmissibility of a nonlinear isolator with high-static-low-dynamic stiffness,

458   *International Journal of Mechanical Sciences*, 55 (2012) 22-29.

459   [21] J. Yang, Y.P. Xiong, J.T. Xing. Dynamics and power flow behavior of a nonlinear

460   vibration isolation system with a negative stiffness mechanism, *Journal of Sound*

461   *and Vibration*, 332 (2013)   167-183.

462   [22] A.D. Shaw, S.A. Neild, D.J. Wagg. Dynamic analysis of high static low dynamic

463   stiffness vibration isolation mounts, *Journal of Sound and Vibration*, 332 (2013)

464   1437-1455.

465   [23] A. Carrella, M.J. Brennan, T.P Waters, K. Shin. On the design of a

466   high-static–low-dynamic stiffness isolator using linear mechanical springs and

467   magnets, *Journal of Sound and Vibration*, 315 (2008) 712–720.

468   [24] W.S. Robertson, M. Kidner, B.S. Cazzolato, A.C. Zander. Theoretical design

469   parameters for a quasi-zero stiffness magnetic spring for vibration isolation,

470   *Journal of Sound and Vibration*, 326 (2009) 88-103.

471   [25] M.M. Khan, D.C. Lagoudas, J.J. Mayes, B.K. Henderson. Pseudoelastic SMA

472   spring elements for passive vibration isolation: Part I Modeling, *Journal of*

473   *Intelligent Material Systems and Structures*. 15 (2004) 415-441.

474   [26] Y. Araki, T. Asai, T. Masui. Vertical vibration isolator having piecewise constant

475   restoring force, *Earthquake Engineering & Structural Dynamics*, 38 (2009)

476   1505-1523.

477   [27] Y. Araki, S. Kawabata, T. Asai, T. Masui. Response of vibration isolated object to

478   ground motions with intense vertical accelerations, *Engineering Structures*, 33

479   (2011) 3610-3619.

480   [28] N. Kikuchi, J.T. Oden, Contact Problems in Elasticity: A Study of Variational

481   Inequalities and Finite Element Methods, SIAM, 1995.

482   [29] D. Cardone, Re-centering capability of flag-shaped seismic isolation systems,

483   Bulletin of Earthquake Engineering 10 (2012) 1267–1284.

484   [30] A.K. Chopra, Dynamic of Structures, 4th edition, Prentice Hall, 2011.

485
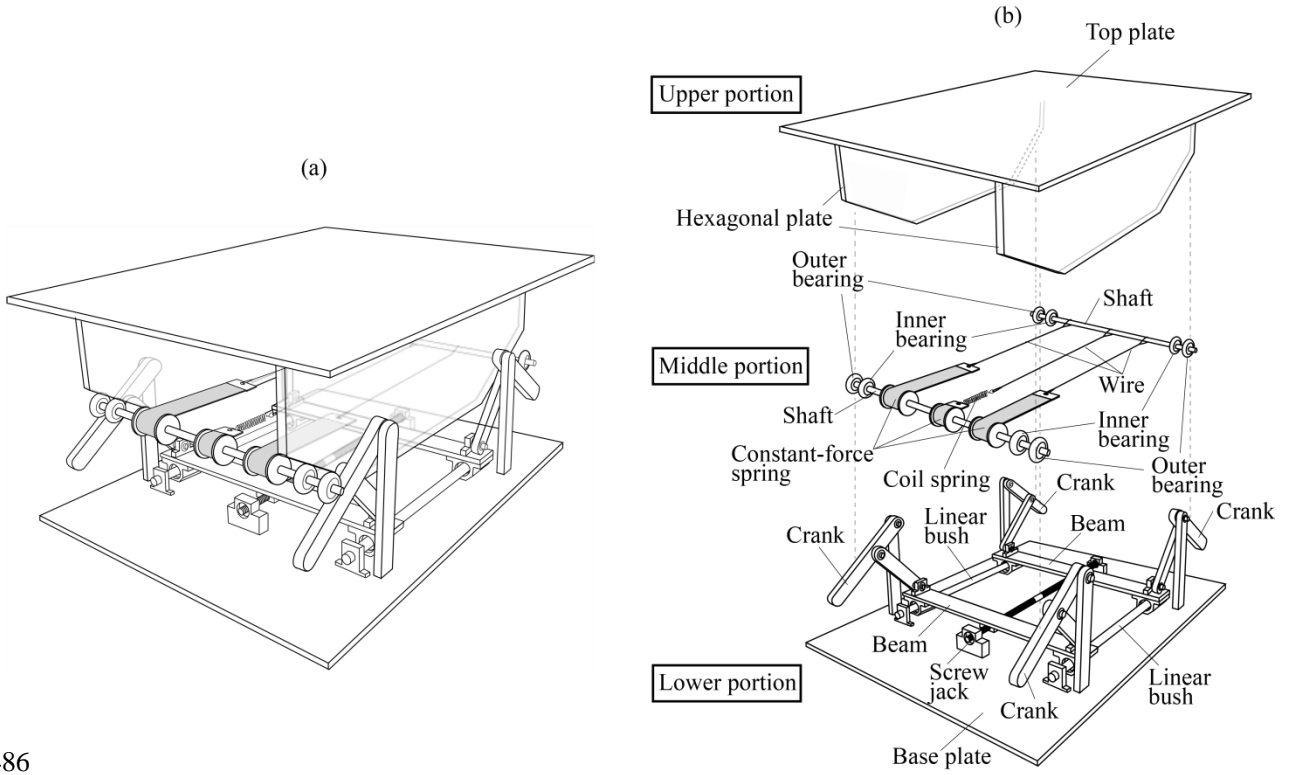
Figure 1: Schematic view of the proposed vibration isolator. (a) Whole view. (b) Each component.
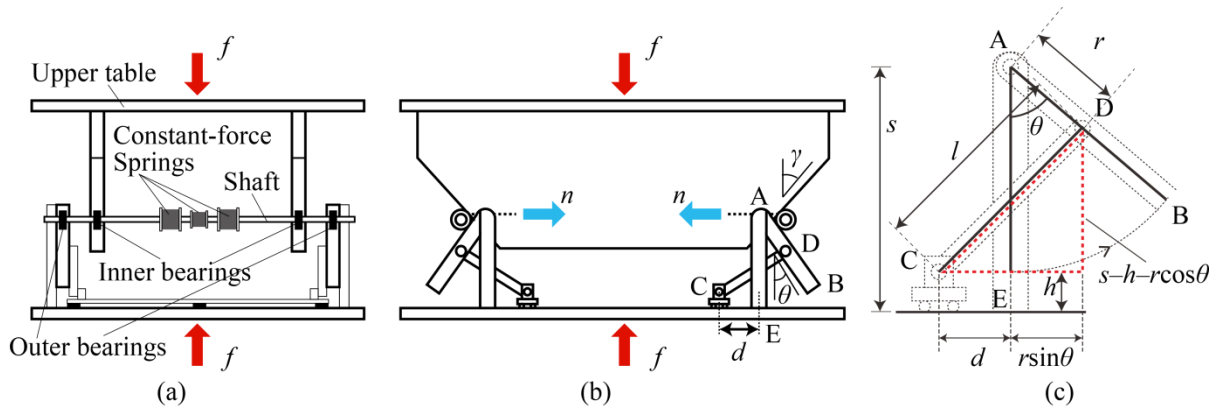
Figure 2: Schematic illustration of the proposed device. (a) Front side. (b) Lateral side. (c) Crank.
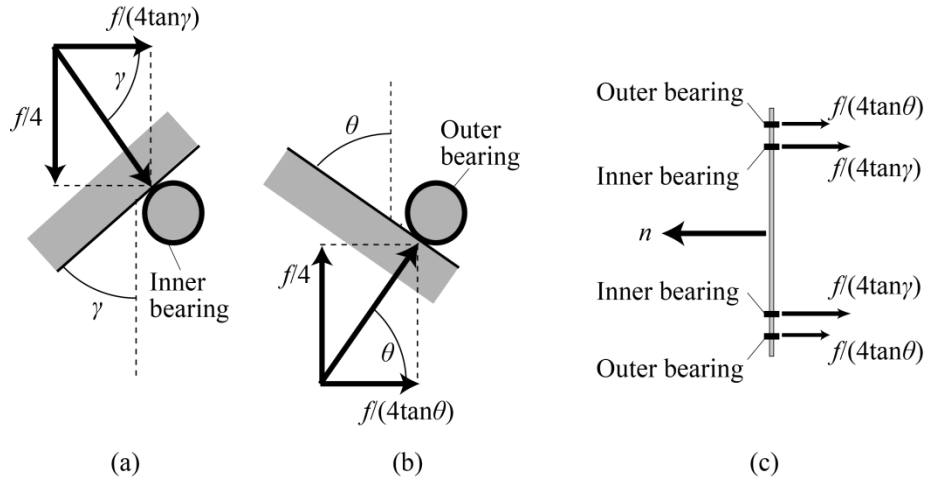
495

496   Figure 3: Internal force on the right shaft. (a) Inner bearing. (b) Outer bearing. (c) Equilibrium

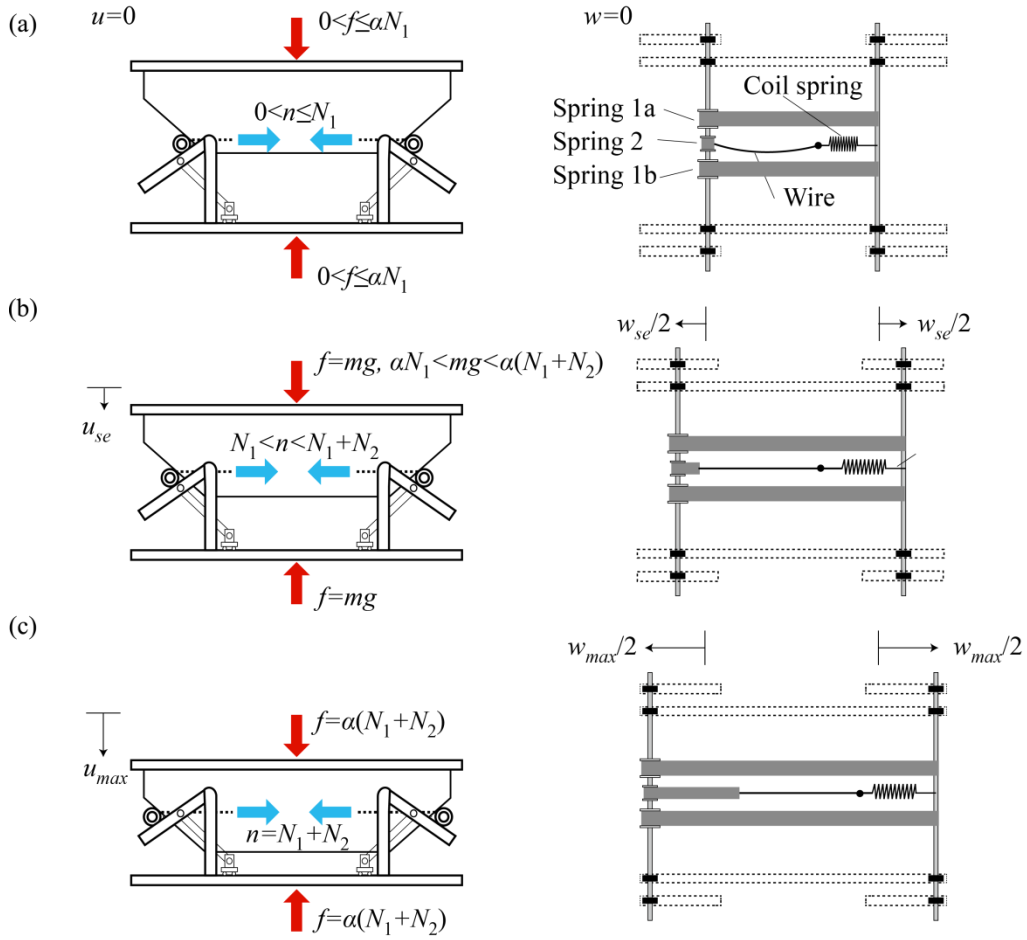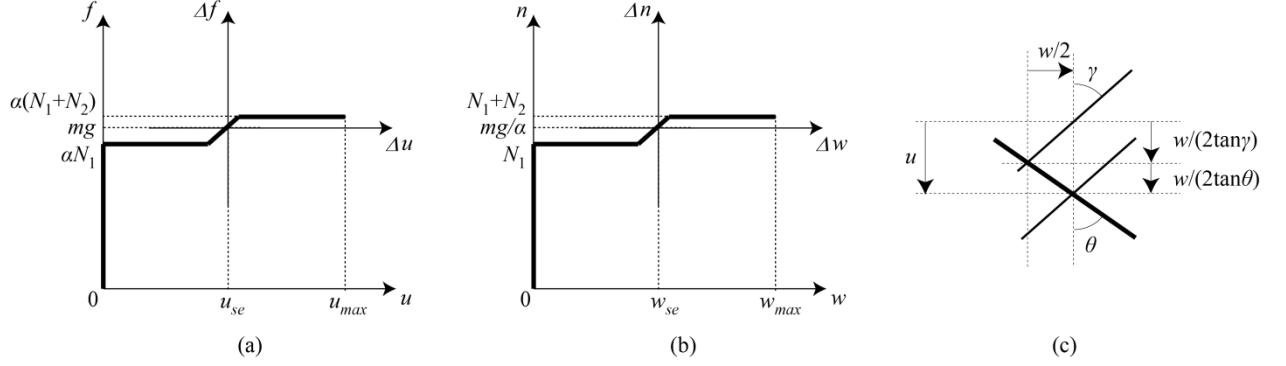497   of horizontal forces acting on the right shaft.

498

499

500   Figure 4: Mechanism for producing nonlinear restoring force. (a) Upper limit position. (b) Static

501   equilibrium position. (c) Lower limit position.

502

503   (a)   (b)   (c)

504 Figure 5: Coordinates. (a) u-f and Δu-Δf. (b) w-n and Δw-Δn. (c) Geometric relationship between u
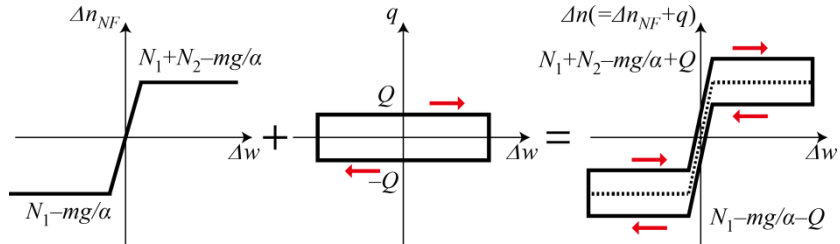
505 and w.

506

507   (a)   (b)
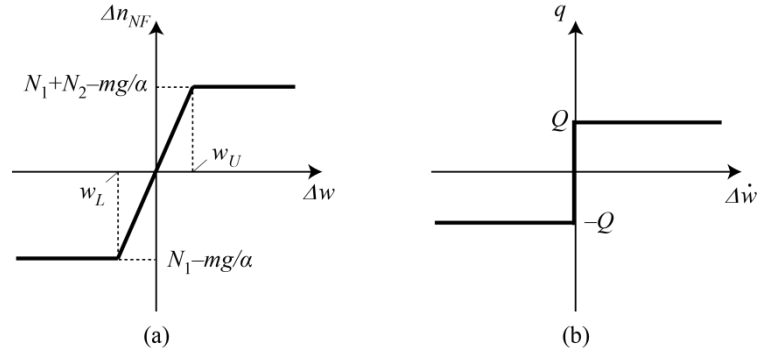
508 Figure 6: Numerical models. (a) Restoring force. (b) Friction force.

509

510

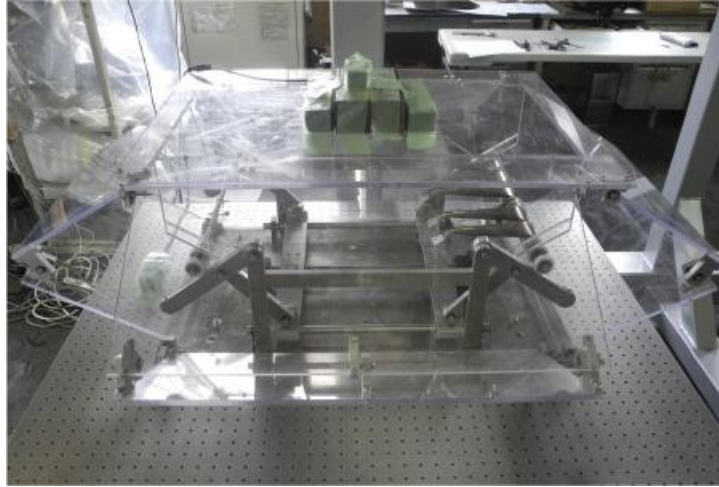511 Figure 7: Schematic illustration of the restoring force model including friction.

512

30

513

Figure 8: Photograph of a prototype of the vibration isolator.
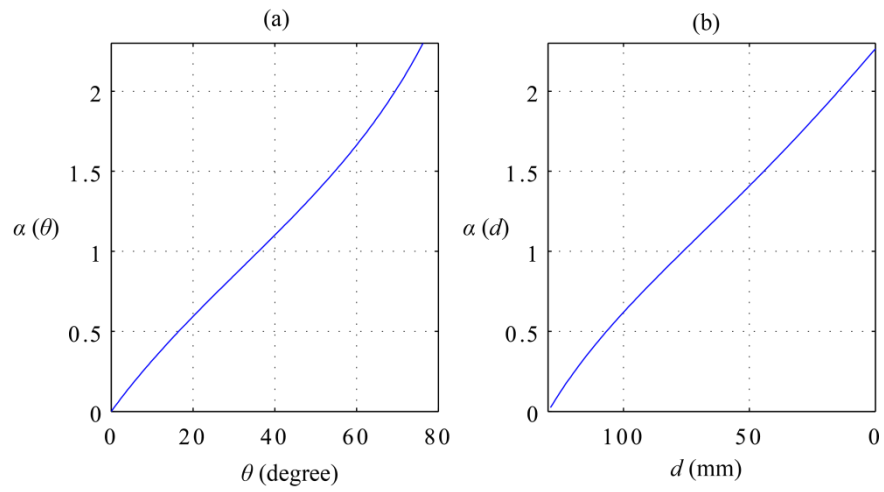
515

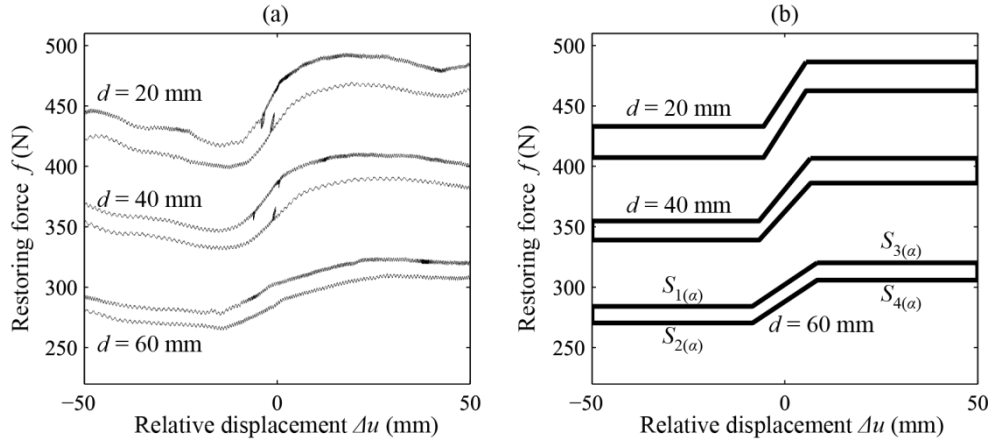517   Figure 9: Amplification factor α. (a) α of θ. (b) α of d.

518

31

Figure 10: Restoring forces for the cases of $d = 60$ mm, $d = 40$ mm, and $d = 20$ mm. (a) Quasi-static loading test results. (b) Numerical models.
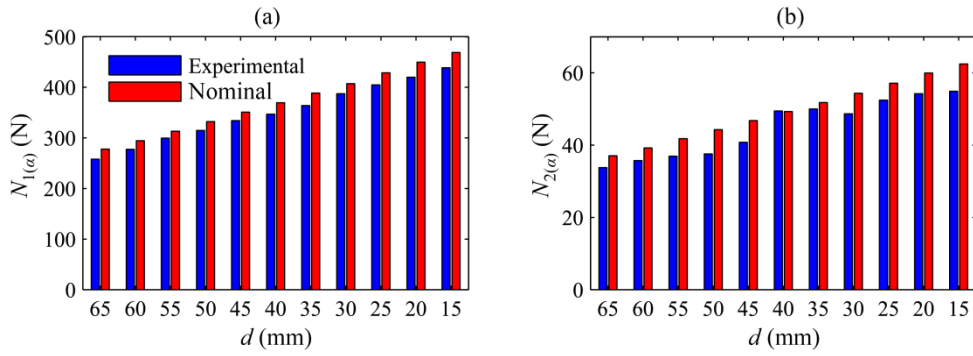

Figure 11: Comparisons between the experimental and nominal capacities of the constant-force springs. (a) $N_{1(\alpha)}$. (b) $N_{2(\alpha)}$.
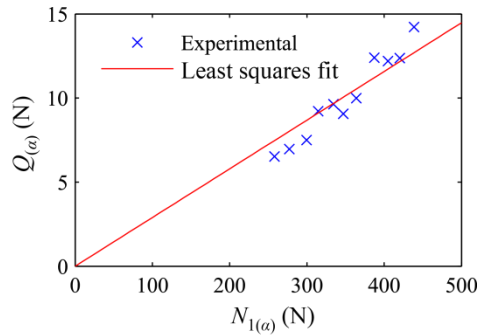
Figure 12: Relationship between $N_{1(\alpha)}$ and $Q_{(\alpha)}$.
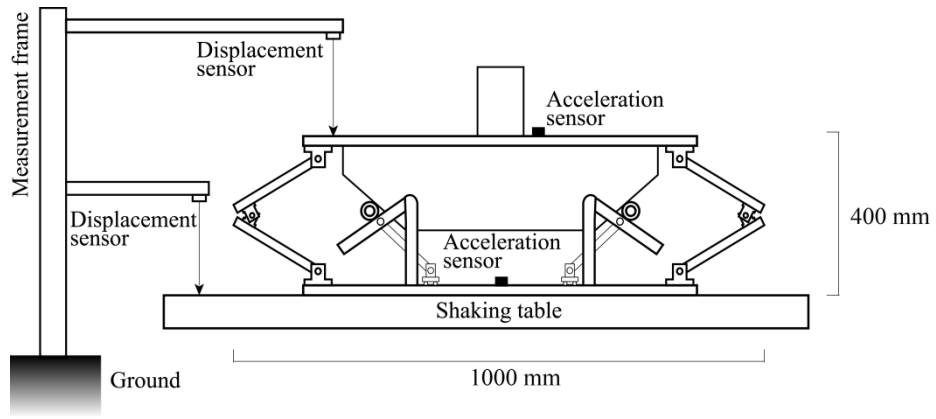
530

531 Figure 13: Experimental setup for the shaking table tests.

532

533
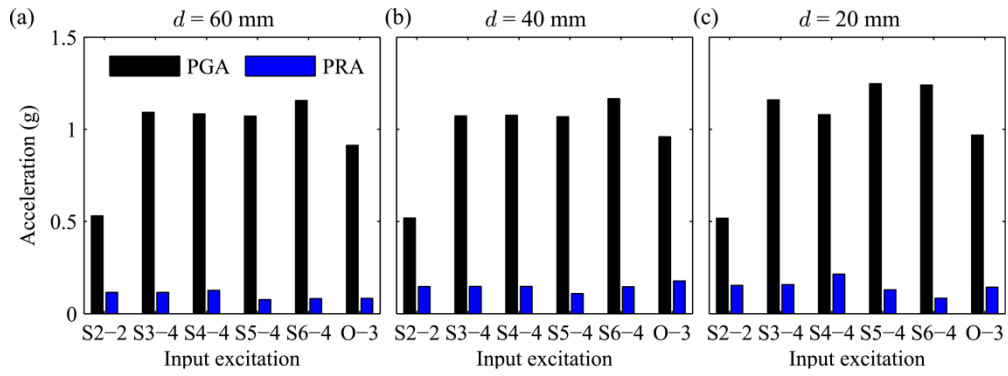
534 Figure 14: Comparisons of peak accelerations measured in shaking table tests. (a) $d = 60$ mm.

535 (b) $d = 40$ mm. (c) $d = 20$ mm.

536

(a)

(b)

537

538   Figure 15: Time histories of shaking table tests for the case of $d = 40$ mm. (a) S4-4. (b) O-3.

539

540

541   Figure 16: Comparisons of time histories between shaking table tests and simulations for the

542   case of d = 40 mm. (a) S4-4. (b) O-3.

543

544

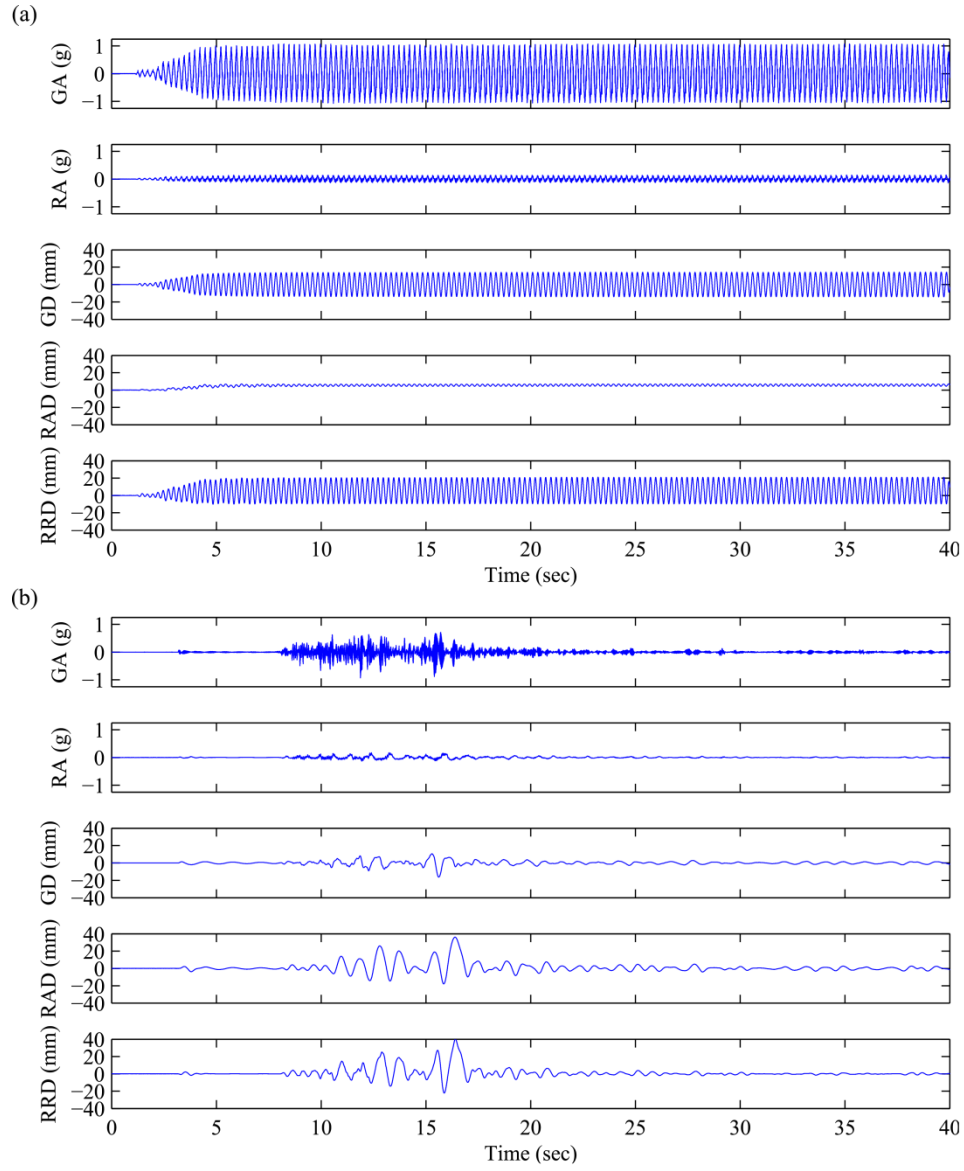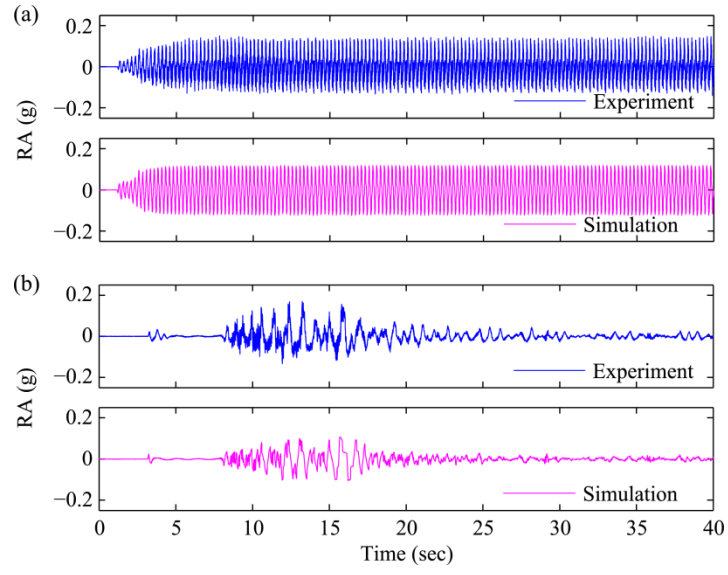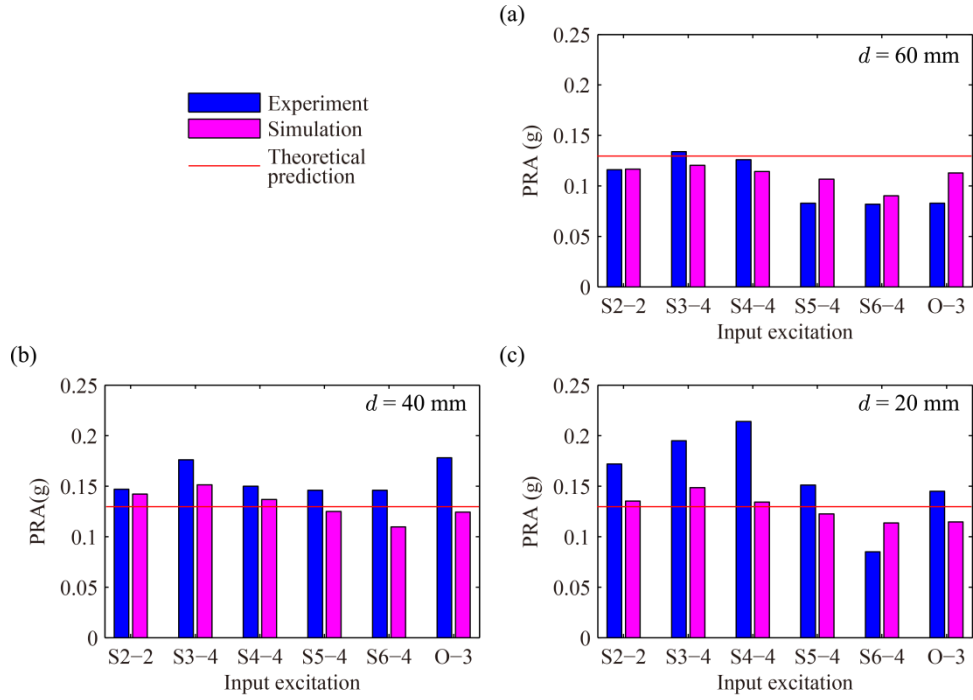545   Figure 17: Comparisons of peak response accelerations. (a) d = 60 mm. (b) d = 40 mm. (c) d =

546   20 mm.

547

35
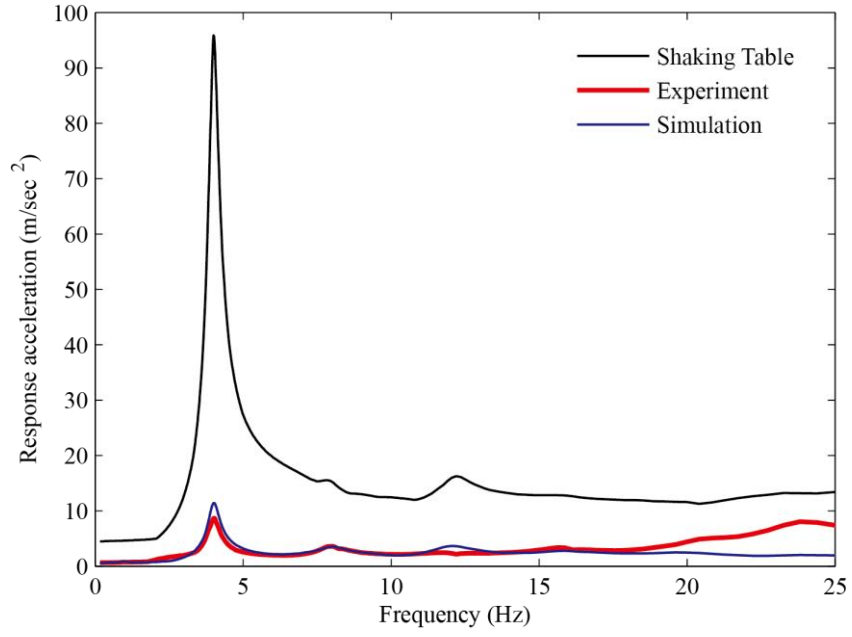
Figure 18: Response acceleration spectra for the case of S4-4 and d = 20 mm.

550

551 Table 1: Reference values of parameters.

d (mm)	α	$N_{1(\alpha)}$ (N)	$N_{2(\alpha)}$ (N)	$Q_{(\alpha)}$ (N)	$u_{R(\alpha)}$ (mm)	$k_{(\alpha)}$ (N/mm)
65	1.18	277.9	37.1	8.0	17.7	2.09
60	1.25	294.4	39.3	8.5	16.7	2.34
55	1.33	313.2	41.8	9.1	15.7	2.65
50	1.41	332.1	44.3	9.6	14.8	2.98
45	1.49	350.9	46.8	10.1	14.0	3.33
40	1.57	369.7	49.3	10.7	13.3	3.70
35	1.65	388.6	51.8	11.2	12.7	4.08
30	1.73	407.4	54.3	11.8	12.1	4.49
25	1.82	428.6	57.1	12.4	11.5	4.97
20	1.91	468.6	60.0	13.0	11.0	5.47
15	1.99	449.8	62.5	13.5	10.5	5.94

552

553 Table 2: Experimental values of parameters.

d	$S_{1(\alpha)}$ (N)	$S_{2(\alpha)}$ (N)	$S_{3(\alpha)}$ (N)	$S_{4(\alpha)}$ (N)	$N_{1(\alpha)}$ (N)	$N_{2(\alpha)}$ (N)	$Q_{(\alpha)}$ (N)	$k_{(\alpha)}$

(mm)								(N/mm)
65	264.1	252.0	298.9	284.9	258.1	33.8	6.5	2.09
60	284.2	270.5	320.3	306.2	277.3	35.7	7.0	2.34
55	306.9	292.3	344.2	328.9	299.6	37.0	7.5	2.65
50	323.3	306.0	362.0	342.4	314.6	37.6	9.2	2.98
45	344.1	324.4	384.4	365.7	334.3	40.8	9.6	3.33
40	354.8	339.1	406.7	386.2	347.0	49.5	9.1	3.70
35	373.4	354.6	424.6	403.5	364.0	50.0	10.0	4.08
30	399.9	374.6	447.7	423.4	387.2	48.7	12.4	4.49
25	417.3	392.4	469.3	445.4	404.9	52.5	12.2	4.97
20	433.0	407.4	486.4	462.5	420.2	54.3	12.4	5.47
15	454.2	422.8	506.2	480.6	438.5	54.9	14.2	5.94

554

555 Table 3: Input excitations.

Name	Input	Intended PGA (g)	Name	Input	Intended PGA (g)
S2-1	2 Hz sine wave	0.25	S5-1	5 Hz sine wave	0.25
S2-2	2 Hz sine wave	0.50	S5-2	5 Hz sine wave	0.50
S3-1	3 Hz sine wave	0.25	S5-3	5 Hz sine wave	0.75
S3-2	3 Hz sine wave	0.50	S5-4	5 Hz sine wave	1.00
S3-3	3 Hz sine wave	0.75	S6-1	6 Hz sine wave	0.25
S3-4	3 Hz sine wave	1.00	S6-2	6 Hz sine wave	0.50
S4-1	4 Hz sine wave	0.25	S6-3	6 Hz sine wave	0.75
S4-2	4 Hz sine wave	0.50	S6-4	6 Hz sine wave	1.00
S4-3	4 Hz sine wave	0.75	O-1	K-NET Ojiya UD	0.50
S4-4	4 Hz sine wave	1.00	O-2	K-NET Ojiya UD	0.75
			O-3	K-NET Ojiya UD	1.00

556

557 Table 4: Comparisons between peak ground accelerations and peak response accelerations (g).

d	60 mm		40 mm		20 mm	
Excitation	PGA	PRA	PGA	PRA	PGA	PRA
S2-1	0.261	0.073	0.274	0.130	0.257	0.122

S2-2	0.531	0.116	0.519	0.147	0.518	0.154
S3-1	0.261	0.054	0.300	0.082	0.271	0.108
S3-2	0.522	0.086	0.525	0.122	0.631	0.129
S3-3	0.809	0.111	0.800	0.134	0.835	0.144
S3-4	1.092	0.116	1.073	0.148	1.159	0.158
S4-1	0.267	0.040	0.264	0.079	0.262	0.075
S4-2	0.537	0.063	0.565	0.077	0.525	0.094
S4-3	0.808	0.088	0.830	0.116	0.817	0.160
S4-4	1.083	0.126	1.076	0.148	1.079	0.214
S5-1	0.273	0.034	0.271	0.044	0.270	0.056
S5-2	0.535	0.046	0.529	0.068	0.532	0.087
S5-3	0.826	0.061	0.804	0.090	0.812	0.116
S5-4	1.071	0.077	1.068	0.109	1.248	0.130
S6-1	0.299	0.034	0.262	0.061	0.260	0.055
S6-2	0.548	0.045	0.614	0.087	0.547	0.070
S6-3	0.874	0.067	0.852	0.133	0.870	0.079
S6-4	1.156	0.082	1.166	0.146	1.240	0.084
O-1	0.429	0.061	0.473	0.146	0.494	0.132
O-2	0.680	0.072	0.706	0.160	0.698	0.133
O-3	0.913	0.083	0.960	0.178	0.968	0.144

558

559   Table 5: Comparisons between peak ground displacements and peak response absolute
560   displacements (mm).

d	60 mm		40 mm		20 mm	
Excitation	PGD	PRAD	PGD	PRAD	PGD	PRAD
S2-1	14.089	6.084	13.691	8.919	13.608	9.647
S2-2	28.213	11.744	27.947	8.106	27.831	9.931
S3-1	6.366	1.622	6.167	2.994	6.092	3.094
S3-2	12.566	2.431	12.552	5.291	12.605	5.341
S3-3	18.883	2.569	18.700	6.697	18.661	6.981
S3-4	25.022	6.841	24.717	6.722	24.503	6.831
S4-1	3.650	1.428	3.573	1.175	3.595	1.209
S4-2	7.250	0.894	7.223	2.784	7.209	2.509
S4-3	10.923	1.219	10.636	4.550	10.863	3.806

S4-4	14.552	1.922	14.248	7.138	14.475	4.650
S5-1	2.341	0.913	2.327	0.613	2.338	0.691
S5-2	4.711	1.116	4.763	1.034	4.694	1.206
S5-3	7.141	1.319	7.081	1.641	7.128	2.066
S5-4	9.358	1.456	9.313	2.384	11.006	2.347
S6-1	1.677	0.344	1.641	0.406	1.663	0.378
S6-2	3.325	0.453	3.320	0.528	3.319	0.491
S6-3	5.009	0.469	5.000	0.978	4.994	1.066
S6-4	6.586	0.563	7.027	1.228	6.630	1.550
O-1	8.163	12.378	8.345	21.709	12.084	28.863
O-2	12.175	13.300	12.267	32.478	12.170	28.922
O-3	16.297	17.122	16.322	35.975	16.211	30.013

561